

Table S1.1. Coefficients used to calculate solubilities Eq. (S1.1) and Schmidt numbers Eq. (S1.4).

	CO ₂	O ₂	N ₂
l	0.996	$\frac{\text{kg/mol}}{e^{V_{\text{ideal}}}}$	$\frac{\text{kg/mol}}{e^{V_{\text{ideal}}}}$
A_1	-60.2409	-58.3877	-59.6274
A_2	93.4517	85.8079	85.7661
A_3	23.3585	23.8439	24.3696
B_1	0.023517	-0.034892	-0.051580
B_2	-0.023656	0.015568	0.026329
B_3	0.0047036	-0.0019387	-0.0037252
	(Weiss, 1974)	(Weiss, 1970)	
C_0	2073.1	1953.4	2206.1
C_1	-125.62	-128.00	-144.86
C_2	3.6276	3.9918	4.5413
C_3	-0.043219	-0.050091	-0.056988
	(as given in Wanninkhof, 1992)		

Supplementary material

S1 Implementation details

S1.1 Auxiliary quantities of gas exchange

The solubility depends on temperature T (in °C) and salinity S , parametrized according to Weiss (1974)

$$L = l \cdot \exp \left(A_1 + A_2 \frac{100\text{K}}{T + T_0} + A_3 \ln \frac{T + T_0}{100\text{K}} + \frac{S}{\text{‰}} \left\{ B_1 + B_2 \frac{T + T_0}{100\text{K}} + B_3 \left(\frac{T + T_0}{100\text{K}} \right)^2 \right\} \right) \frac{\text{mol}}{\text{kg} \cdot \text{atm}} \quad (\text{S1.1})$$

with species-dependent coefficients from Tab. S1.1. For CO₂, the additional factor l allows to use this solubility with partial pressure rather than fugacity (temperature dependence neglected); for the other gases it converts from Bunsen solubility.

The atmospheric partial pressure p_a of a gas is proportional to its dry-air molar mixing ratio X via

$$p_a = X (p_{\text{baro}} - p^{\text{H}_2\text{O}}) \quad (\text{S1.2})$$

The correction for water vapor pressure (to get the dry-air pressure) is calculated from SST and SSS as (Weiss and Price, 1980)

$$p^{\text{H}_2\text{O}} = p_{\text{baro}} \cdot \exp \left(24.4543 - 67.4509 \frac{100\text{K}}{T + T_0} - 4.8489 \ln \frac{T + T_0}{100\text{K}} - 0.000544 \frac{S}{\text{‰}} \right) \quad (\text{S1.3})$$

The Schmidt number depends on T according to (Wanninkhof (1992) based on data by Jähne et al. (1987))

$$Sc = C_0 + C_1 \left(\frac{T}{\text{°C}} \right) + C_2 \left(\frac{T}{\text{°C}} \right)^2 + C_3 \left(\frac{T}{\text{°C}} \right)^3 \quad (\text{S1.4})$$

with coefficients from Tab. S1.1 (coefficients are valid for $S = 35\text{‰}$, i.e., any salinity dependence is neglected). The reference Schmidt number (arbitrary due to the scaling of Γ in Eq. (A2)) is

$$Sc^{\text{Ref}} = 660 \quad (\text{S1.5})$$

S1.2 Treatment of ice-covered areas

Sea-air gas exchange is very different in ice-covered areas. While sea ice prevents sea-air exchange as considered above, there are tracer fluxes through cracks (leads), gas bubbles and fresh-water dilution from melting ice, etc. (e.g., Takahashi et al. (2009) account for this by reducing sea-air exchange in ice-covered areas to 10% of the open-ocean fluxes, rather than zero fluxes.) As further second-order effects, the ice smoothes the wave field and thus affects gas exchange; large temperature gradients in

the overlying atmosphere affect the local subgrid scale atmospheric circulations; the transport model clearly cannot resolve the atmospheric Arctic boundary layer and may have numerical distortions close to the poles.

An additional practical problem is that many of our driving fields (MLD, Revelle factor, mean DIC, etc.) are not available at high northern latitudes. On the other hand, however, the contribution of sea-air fluxes from ice-covered regions is small in the global context.

As a pragmatic solution, we therefore

- scale all piston velocities by a factor related to the instantaneous ice-free fraction,

$$0.9 \cdot \varepsilon + 0.1 \tag{S1.6}$$

- missing driving fields are extrapolated from data-covered regions towards the poles;
- declare all pixels where time-mean ice-free area is less than 50% as inactive; in these regions, ocean quantities are not adjusted in the inversion, but kept at their a-priori values calculated from Takahashi et al. (2009) climatology.

Areas without driving fields also exist along the coasts and in marginal seas. As for the ice-covered areas, fields are extrapolated from open-ocean areas towards West or East, respectively.

S2 Sensitivity cases

In addition to the sensitivity cases mentioned in Sect. 2.5.2 shown as grey band in Fig. 4, various other tests have been performed. Unless mentioned otherwise, they only change the fitted p^{CO_2} field (and thus the sea-air flux) by the same order of magnitude as the grey band or less.

- Increasing the **a-priori uncertainty** by a factor 2 or 4, or decreasing it by a factor 2 (part of grey sensitivity band).
- Shortening the **a-priori spatial correlation length** by a factor 1/3 (part of grey sensitivity band).
- Changing the **atmospheric CO₂ concentration for the gas exchange** (X^{CO_2}). This was done by (1) performing a fit to the atmospheric CO₂ data using the result of run **SFC** as fixed ocean fluxes (2) creating X^{CO_2} by a forward transport model run from the resulting a-posteriori fluxes, (3) repeating run **SFC** using this X^{CO_2} field. Actually, this procedure could be repeated (“outer loop”) to ensure that X^{CO_2} is consistent with the flux estimates, however the sensitivity of the results to X^{CO_2} is low anyway.
- Replacing **seasonally varying mixed-layer depth** h by its temporal mean. Contrary to what may be expected, the sensitivity of p^{CO_2} is very low; the sensitivity of $f_{\text{int}}^{\text{DIC}}$ is larger, mainly because the history flux vanishes for constant h ; however the sensitivity of the PO₄ field is very low again because the history flux vanishes for both DIC and PO₄.
This low sensitivity to the seasonality of mixed-layer depth indicates that its missing interannual variations should not be a large problem for future applications of the diagnostic scheme to IAV.
- Increasing or decreasing the **gas exchange** (scaling Γ) by a factor 2. The sensitivity of p^{CO_2} is low (it does exist because the time constant of the budget equation changes), but the sea-air fluxes are of course scaled roughly proportionally to Γ .
- Omitting certain processes in the carbonate chemistry and DIC budget (**alkalinity dependence, salinity dependence, freshwater dilution effect**). There is little change to the estimated p^{CO_2} field, but the ocean-internal fluxes, and thus the PO₄ field, change more strongly. Of course, omitting these processes is expected to deteriorate the result, but the test demonstrates that PO₄ is sensitive to errors in the respective parametrization and its input driving fields (A , S , T) which are hard to quantify.
- Allowing interannual variations in the adjustable ocean-internal fluxes (rather than seasonal variations only). Due to the strongly varying data availability (Fig. S7.3), this leads to strong temporal excursions in the p^{CO_2} field, often exceeding the seasonal amplitude. The mean seasonal cycle of p^{CO_2} is higher in the temperate regions, and lower in the high-latitude regions, of both hemispheres. Surprisingly, in the Northern high-latitude Pacific and Atlantic, the mean seasonal cycle agrees almost perfectly to the Takahashi et al. (2009) climatology, quite unlike the standard result. As the strong variations in this sensitivity case do not appear to be realistic, the interpretation of this finding is difficult.
- Skipping SOCAT data values from all pixels where the first and the last existing measurement are within less than 1 year. Sensitivity very low in most regions, except for North Pacific (where the result is more close to the LDEO-based result of Fig. S6.1), the temperate North Atlantic due to the missing Mediterranean values, and the Tropical Indian.
- Skipping **coastal values** in the SOCAT data set (e.g., all values from locations shallower than 400m), or also including values less than 200 μatm or larger than 600 μatm (normally skipped, Tab. 1); (sensitivity very low).
- Transferring the SOCAT data values from their **local sea surface temperature** (as given in the data set) to that of its grid cell in our T field, i.e., to the value that should have been measured if T was true. The sensitivity is low, except for the Tropical Atlantic.
- **Data density weighting** of the SOCAT data, similar to that of the atmospheric data (Rödenbeck, 2005). The weighting was done such that averages over months and $\approx 150\text{km}$ areas have similar weight in the cost function (sensitivity very low).
- Omitting the **fugacity factor** in the data (sensitivity very low).

S3 The history flux

Here we show analytically that the history flux f_{hist} according to Eq. (A18) compensates long-term imbalances of the tracer budget Eq. (A16) arising from covariance between tracer concentration C and mixed-layer depth h (“seasonal rectification”).

Consider the mixed-layer concentration of any tracer, e.g. $C = C_{\text{m}}^{\text{DIC}}$. Summarizing all fluxes other than the history flux into f , the budget equation Eq. (A16) is

$$\frac{dC}{dt} = \frac{1}{h\rho} (f + f_{\text{hist}}) \quad (\text{S3.1})$$

The history flux had been defined as (Eq. (A18))

$$f_{\text{hist}}(t) = \rho \cdot \left(C(t_{\text{prev}}) - C(t) \right) \cdot \Theta \left(\frac{dh}{dt} \right) \quad (\text{S3.2})$$

with $t_{\text{prev}} = t_{\text{prev}}(t)$ giving the previous time when the mixed layer was as deep as at t , i.e.,

$$h(t_{\text{prev}}(t)) = h(t) \quad (\text{S3.3})$$

From the mixed-layer concentration C (tracer amount per unit water mass) we consider the total tracer amount in the mixed layer column (amount per ocean surface area),

$$M = \rho h \cdot C \quad (\text{S3.4})$$

Its time-rate of change is

$$\frac{dM}{dt} = \rho h \cdot \frac{dC}{dt} + C \cdot \rho \frac{dh}{dt} \quad (\text{S3.5})$$

We consider a time period starting at a time t_- when the mixed layer is at a depth h_d , then shoals until reaching a minimum depth h_s at an intermediate time t_0 , and then deepens until again reaching depth h_d at time t_+ . During shoaling ($t_- \leq t \leq t_0$), the total tracer amount changes as

$$\frac{dM}{dt} = f(t) + C(t) \cdot \rho \frac{dh}{dt} \quad (\text{S3.6})$$

(substituting Eqs. (S3.1) and (S3.2) into Eq. (S3.5), and considering that the history flux is zero then). During deepening ($t_0 \leq t \leq t_+$), we have

$$\frac{dM}{dt} = f(t) + C(t_{\text{prev}}(t)) \cdot \rho \frac{dh}{dt} \quad (\text{S3.7})$$

The cumulative changes in tracer during shoaling and deepening are then

$$\begin{aligned} M(t_0) - M(t_-) &= \int_{t_-}^{t_0} f(t) dt + \underbrace{\int_{t_-}^{t_0} C(t) \cdot \rho \frac{dh}{dt} dt}_{\int_{h_d}^{h_s} C(t(h)) \cdot \rho dh} \\ M(t_+) - M(t_0) &= \int_{t_0}^{t_+} f(t) dt + \underbrace{\int_{t_0}^{t_+} C(t_{\text{prev}}(t)) \cdot \rho \frac{dh}{dt} dt}_{\int_{h_s}^{h_d} C(t_{\text{prev}}(h)) \cdot \rho dh} \end{aligned} \quad (\text{S3.8})$$

In the second integrals, the independent integration variable has been transformed from t to h , possible because $h(t)$ is bijective within each part of the considered time interval. The new form reveals that the two integrands are in fact equal: $t(h)$ in the upper line (during shoaling) is identical to $t_{\text{prev}}(h)$ in the lower line. The integrals however have opposite sign because the integration limits are exchanged. Therefore, they cancel on summing both lines of Eq. (S3.8), giving

$$M(t_+) - M(t_-) = \int_{t_-}^{t_+} f(t) dt \quad (\text{S3.9})$$

Thus the total change in tracer amount during the considered time period only depends on the fluxes f , while the covariance effects have been cancelled by the history flux: Without the history flux, the lower line of Eq. (S3.8) would not involve $C(t_{\text{prev}})$

but $C(t)$ from the time interval after t_0 , which is in general different from $C(t)$ before t_0 , leading to a spurious net effect of considerable size.

The h climatology used here represents an unimodal cycle of shoaling and deepening; thus the argumentation applies directly. If the mixed-layer is shoaling and deepening multiple times, the yearly cycle needs to be subdivided into several shoaling/deepening periods that can be suitably paired according to the relation of t during deepening and the corresponding $t_{\text{prev}}(t)$ during shoaling.

S4 Testing the retrieval capacity of the atmospheric data (for run ATM)

Analogously to Appendix B, we tested the ability of the atmospheric data at the available measurement sites to constrain p^{CO_2} (or flux) seasonality: Synthetic atmospheric data were generated by a forward run of the atmospheric transport model using fluxes calculated from the Takahashi et al. (2009) climatology (plus fossil fuel emissions and land exchange as in the prior, i.e., no seasonality over land). The comparison between the fit to these synthetic data and the known “truth” was not only done in terms of p^{CO_2} but also in terms of land-air and sea-air fluxes.

The model is largely able to retrieve region-to-region differences of the known “truth” from the atmospheric information (Fig. S4.1). In some regions (e.g., North Pacific) the fit is only good in the run with the least tight prior. In other regions (e.g., the South temperate regions), in contrast, more tight priors are needed to damp spurious signals. The sensitivity to the prior tightness indicates that the fit to (synthetic) atmospheric data is less robust, compared to the fit to p^{CO_2} data. However, in a changed system where the land-atmosphere exchange is fixed (i.e., no adjustable degrees of freedom over land, such that the land fluxes already coincide with the “truth”), this sensitivity becomes much smaller (not shown), indicating that the limited robustness is to large part related to shifts of signals between land and ocean. Consistently, synthetic runs with less tight priors (but original system) also show less spurious variability attributed to land fluxes (not shown).

To investigate this land-ocean crosstalk further, a complementary synthetic run was performed, using a different “truth” having zero (constant) ocean-atmosphere fluxes but seasonal land fluxes (taken from the BiomeBGC biosphere model, which is similar in seasonality to the normal atmospheric CO_2 inversion estimates). As expected, the fit to the synthetic data calculated from this “truth” leads to variability also over the ocean (not shown). Though the amplitude of this spurious ocean variability is comparable to the range from the sensitivity to prior tightness (confirming the paragraph above), it is considerably smaller than the signals themselves (e.g., according to Takahashi et al. (2009)), indicating that the density of the atmospheric station network is actually sufficient to separate land and ocean. In particular, the error amplitude is much smaller than the difference between the p^{CO_2} -based (SFC) and atmosphere-based (ATM) results, especially in the region of the largest discrepancy (North Pacific). Thus this discrepancy cannot be explained by land-ocean crosstalk from limited information in the atmospheric data.

However, land-ocean crosstalk can also arise from errors of the modelled atmospheric transport: If some site is influenced by land signals in reality, but by ocean signals in the model, the inversion will try to match the data from this station by wrongly adjusting ocean rather than land fluxes. Support of this assumption comes from the fact that the discrepancy in the North Pacific is larger when using the coarser-resolution transport model whose errors are likely larger.⁷

⁷We considered whether the suite of TransCom-3L3 inversion results (done by various groups using different transport models but also different inversion methodologies) could be used to reveal such transport model errors. TransCom-3L3 results comprise largely different seasonal cycles, also in the North Pacific. Conclusions from this inter-comparison on possible model errors are difficult, however, also because some of the inversions use the Takahashi et al. (2009) climatology as Bayesian prior.

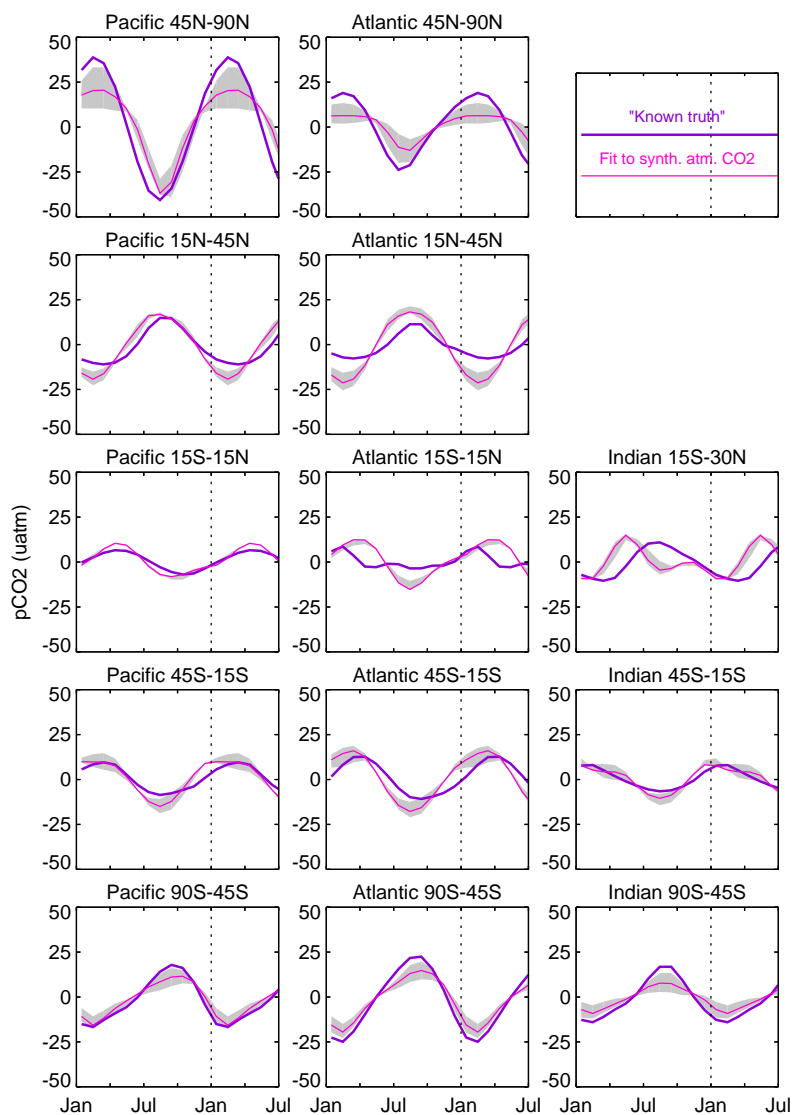


Fig. S4.1. Fit of the diagnostic scheme to synthetic atmospheric CO₂ data, created from a forward run of the atmospheric transport model using sea-air fluxes calculated from the Takahashi et al. (2009) climatology and fluxes identical to the prior on land (constant Net Ecosystem Exchange plus fossil fuel emissions). For computational efficiency, a coarser version of the transport model has been used (for both forward run and inversion). The grey band gives the sensitivity to the strength of the Bayesian prior, with looser priors leading to closer match of the “known truth”.

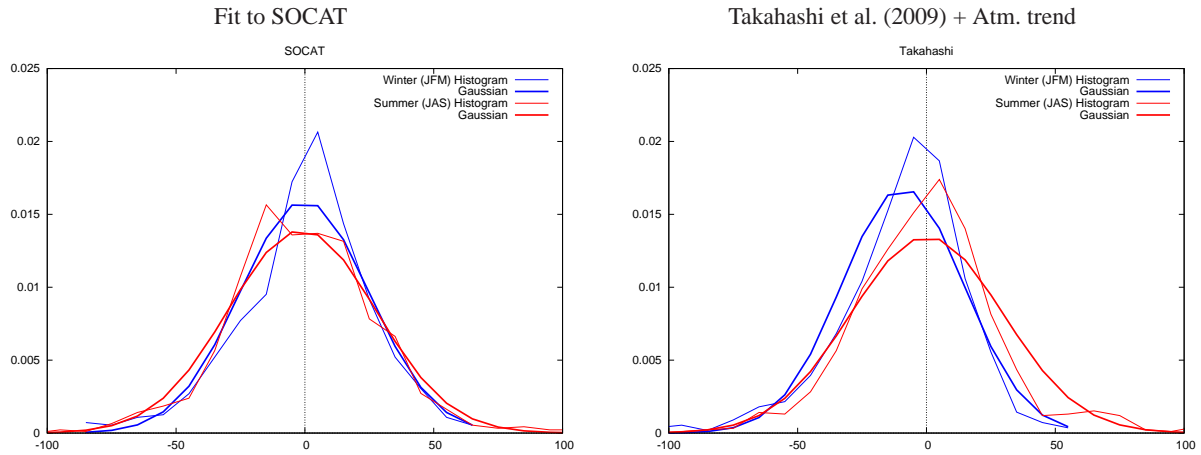


Fig. S5.1. Histograms of p^{CO_2} residuals (μatm) against SOCAT data. Left and right columns refer to the two cases shown in Fig. 4. Thin lines show the relative abundance (within bins of $10\mu\text{atm}$) of differences between the respective field and the SOCAT value over all pixels from the North Pacific (North of 45°) and all time steps where data exist and which lie in winter (JFM, blue), summer (JAS, red). Respective thick lines give a Gaussian of the same mean and standard deviation.

S5 Residuals

Fig. 5 and Fig. 8 already illustrated how the diagnostic model fits the SOCAT data at example locations. To more systematically judge the success of the fit and investigate the differences of the results to the Takahashi et al. (2009) climatology (Fig. 4), we look at the differences of the estimated p^{CO_2} fields and the data at those locations/times where SOCAT data points exist. Fig. S5.1 (left) gives histograms of these residuals within the North Pacific region as example (where differences in Fig. 4 are largest). The mean of these residuals is close to zero, and they are nearly Gaussian distributed, as required mathematically. There is very small seasonal bias between winter and summer. From a similar calculation, Fig. S5.1 (right) shows the difference between Takahashi et al. (2009) (monthly climatology plus the atmospheric trend from $p_a^{\text{CO}_2}$, Eq. (S1.2)) and the SOCAT data points. The climatology is smaller in winter by about $10\mu\text{atm}$ than SOCAT, consistent with the difference to the SOCAT-based fit (Fig. 4, upper left).

A spatial picture of the biases is given in Fig. S5.2. In most areas, mean residuals of the fit are within $\pm 5\mu\text{atm}$ (grey pixels) or scattered in both directions, both year-round and in individual seasons (left panels). Comparing the JFM and JAS residuals, there is little seasonal bias except for small spots off western South America and in the temperate South Atlantic. Differences of the climatology and SOCAT values in mean and seasonal amplitude (right panels) are more systematic in some regions, especially the high Northern areas, as well as the tropical and South Pacific. Note that differences in the tropical Pacific are partially related to the fact that Takahashi et al. (2009) represents a non-El Niño climatology while all SOCAT values have been used. The comparison is consistent with the differences in Fig. 4. (Note that the largest differences between our results and Takahashi et al. (2009) occur in areas hardly covered by data –northernmost Pacific and Mediterranean– and therefore are not well seen in Fig. S5.2, compare however Fig. S7.1).

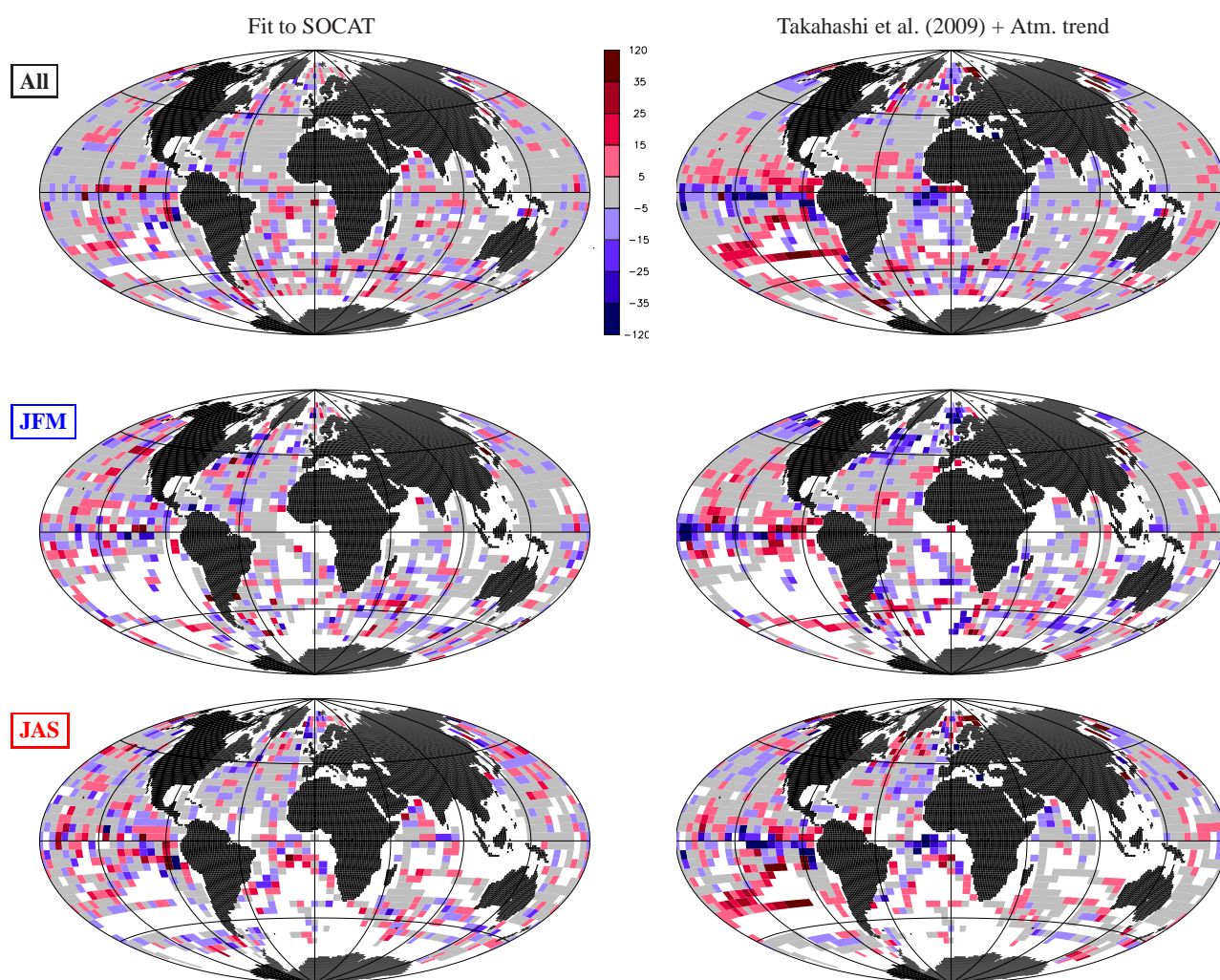


Fig. S5.2. Maps of p^{CO_2} residuals (μatm) against SOCAT data. Left and right columns refer to the two cases shown in Fig. 4. For each pixel, the difference between the respective field and the SOCAT value is shown, averaged over all time steps where data exist (top line). In the middle and bottom, averages have been restricted to (northern) winter (JFM) and summer (JAS), respectively. White areas do not have SOCAT data. (Note that the calculation is done on TM3 grid, i.e., SOCAT values have been averaged over pixels and daily time steps as used in the fit, and Takahashi et al. (2009) has been grid-converted, which may slightly exaggerate the mismatch for the Takahashi et al. (2009). Further, the atmospheric trend has been added to the Takahashi et al. (2009) climatology to avoid unduly large residuals in years away from 2000.)

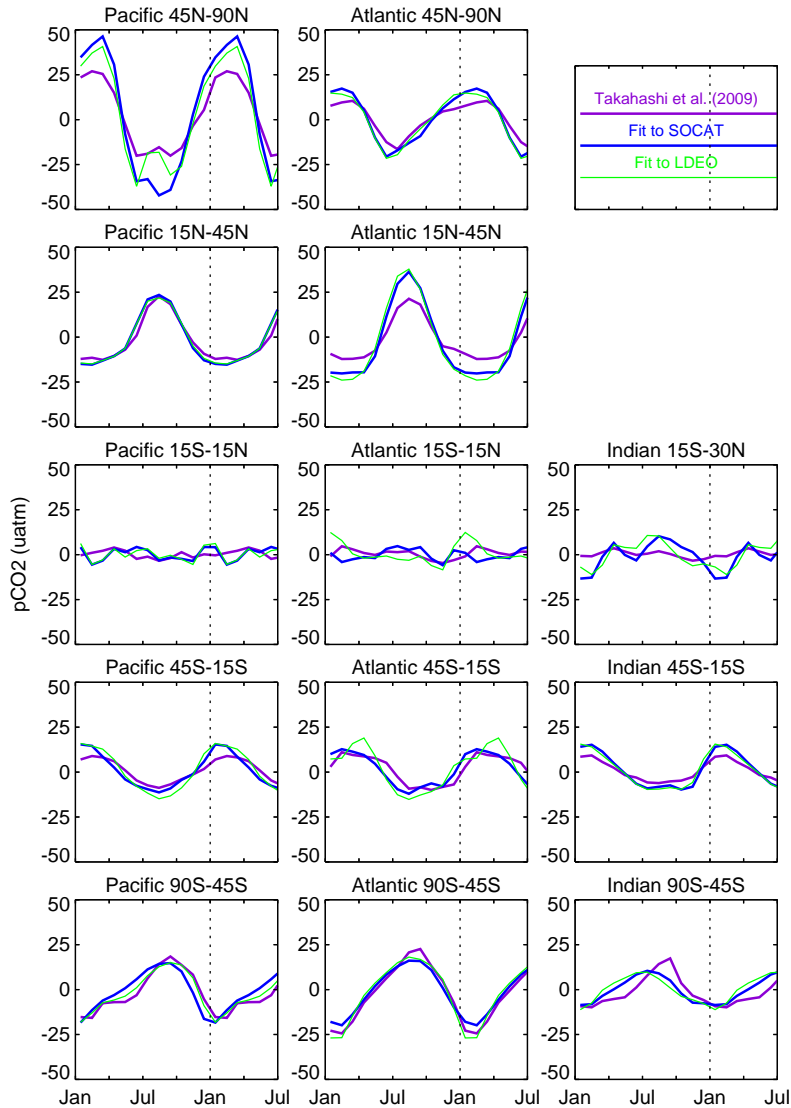


Fig. S6.1. Seasonality of p^{CO_2} as Fig. 4, additionally compared to the fit of the diagnostic scheme to LDEO data (Takahashi et al., 2010).

S6 Fit to the LDEO data base

Partly, the differences between our results and the Takahashi et al. (2009) climatology (Fig. 4) can be traced to the fact that the climatology is based on a different set of data points (the LDEO data set, Takahashi et al., 2010): When fitting the diagnostic scheme to p^{CO_2} values from the LDEO data base rather than to SOCAT, the results get closer to the climatology in many regions (Fig. S6.1), in particular in the North Pacific where Fig. 4 revealed largest differences. Note that the set of LDEO data points used in the fit here is not exactly the same as that used in the Takahashi et al. (2009) climatology, because our fit can only use the data from the inversion period and because the Takahashi et al. (2009) climatology excludes El Niño and coastal values.

There are differences between the fit of the diagnostic scheme to SOCAT or LDEO also in other regions. Most of these (e.g., in the temperate South Atlantic) arise because the data density in LDEO is smaller than in SOCAT: Synthetic-data tests analogous to Fig. 10 reveal that LDEO's density gives a weaker constraint on p^{CO_2} seasonality there (not shown).

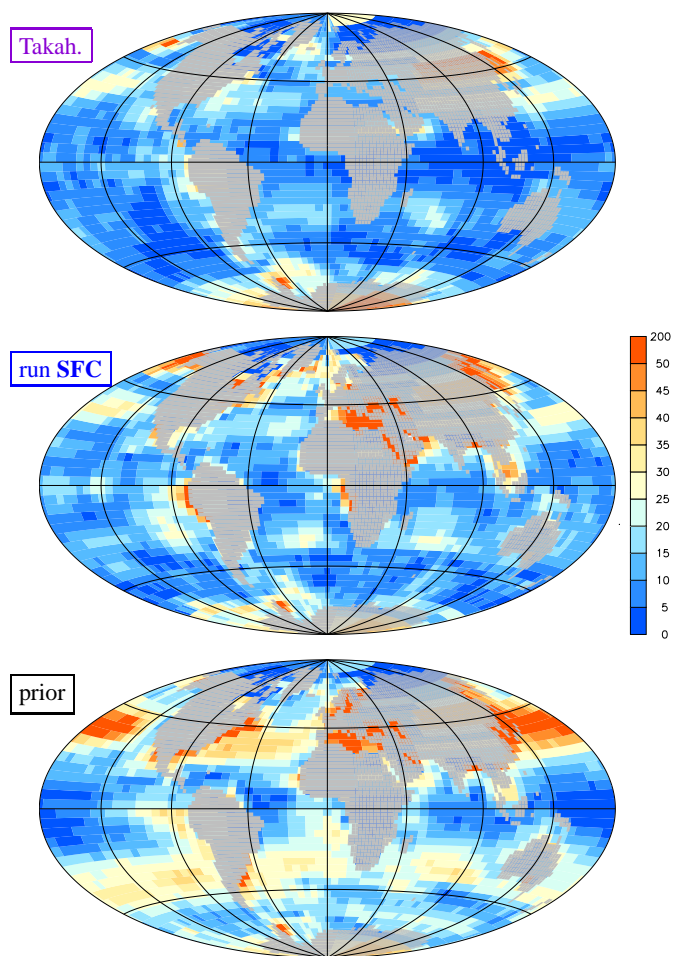


Fig. S7.1. Amplitude of the mean seasonal cycle of surface-ocean CO₂ partial pressure (µatm, identical color scale). Top: Takahashi et al. (2009) (regridded and extrapolated towards the coasts and marginal seas); middle: as estimated by fitting the diagnostic scheme to the SOCAT data (run **SFC**, as Fig. 3); bottom: prior. The amplitude is given as temporal standard deviation of the monthly mean $p_m^{\text{CO}_2}$ at each pixel.

S7 Additional figures

A number of figures are added here to give background information on specific aspects.

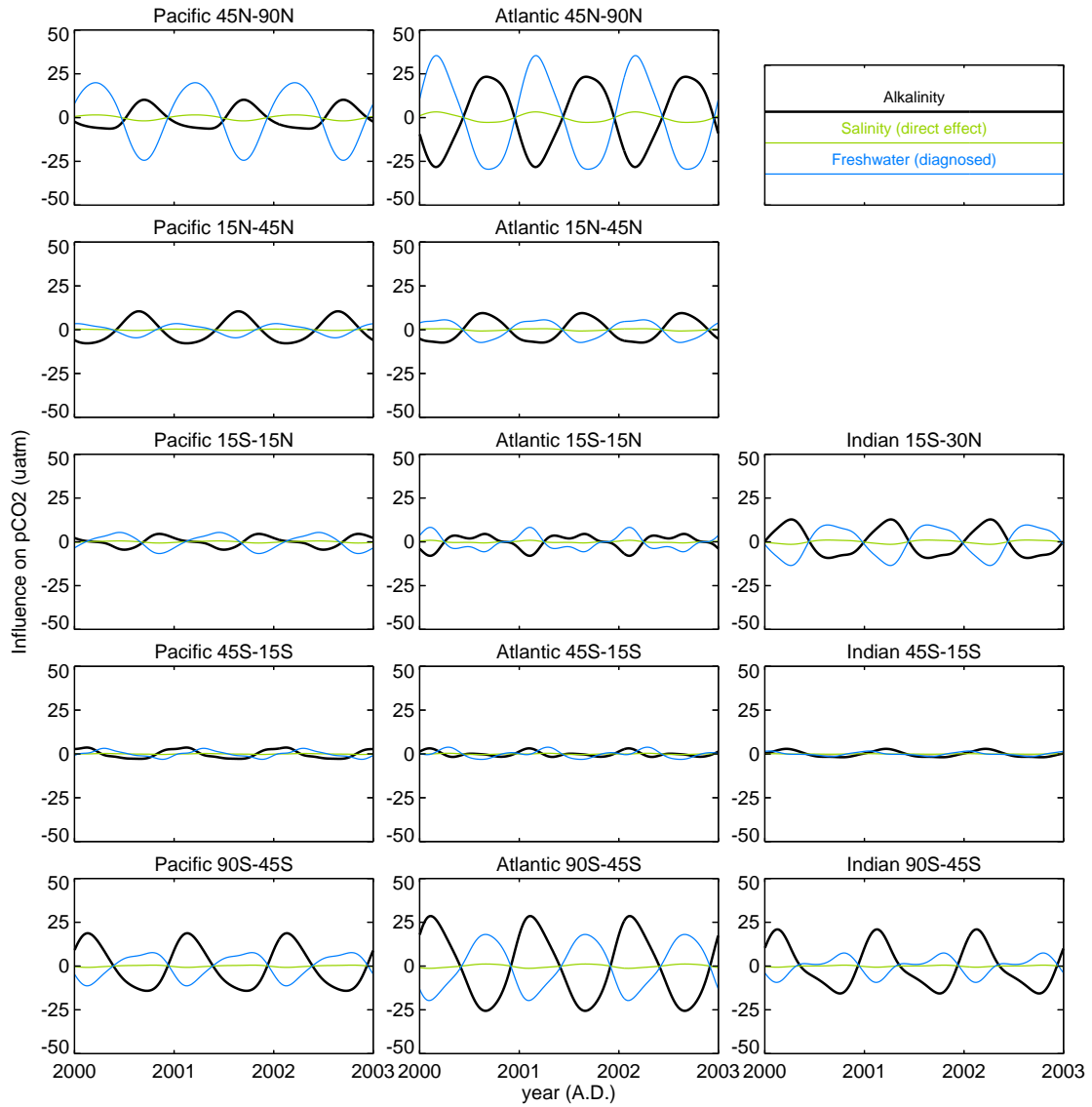


Fig. S7.2. Contributions to the $p_{\text{m}}^{\text{CO}_2}$ seasonality from variations in Alkalinity (black), salinity (direct effect on chemical equilibrium only, green), and freshwater dilution of DIC (calculated in the scheme through $f_{\text{frw}}^{\text{DIC}}$, Eq. (A17), but approximated here by $\frac{\partial p_{\text{m}}^{\text{CO}_2}}{\partial C_{\text{m}}^{\text{DIC}}} \frac{C_{\text{m}}^{\text{DIC,LT}}}{S^{\text{LT}}} (S - S^{\text{LT}})$, blue). Three arbitrary years are shown.

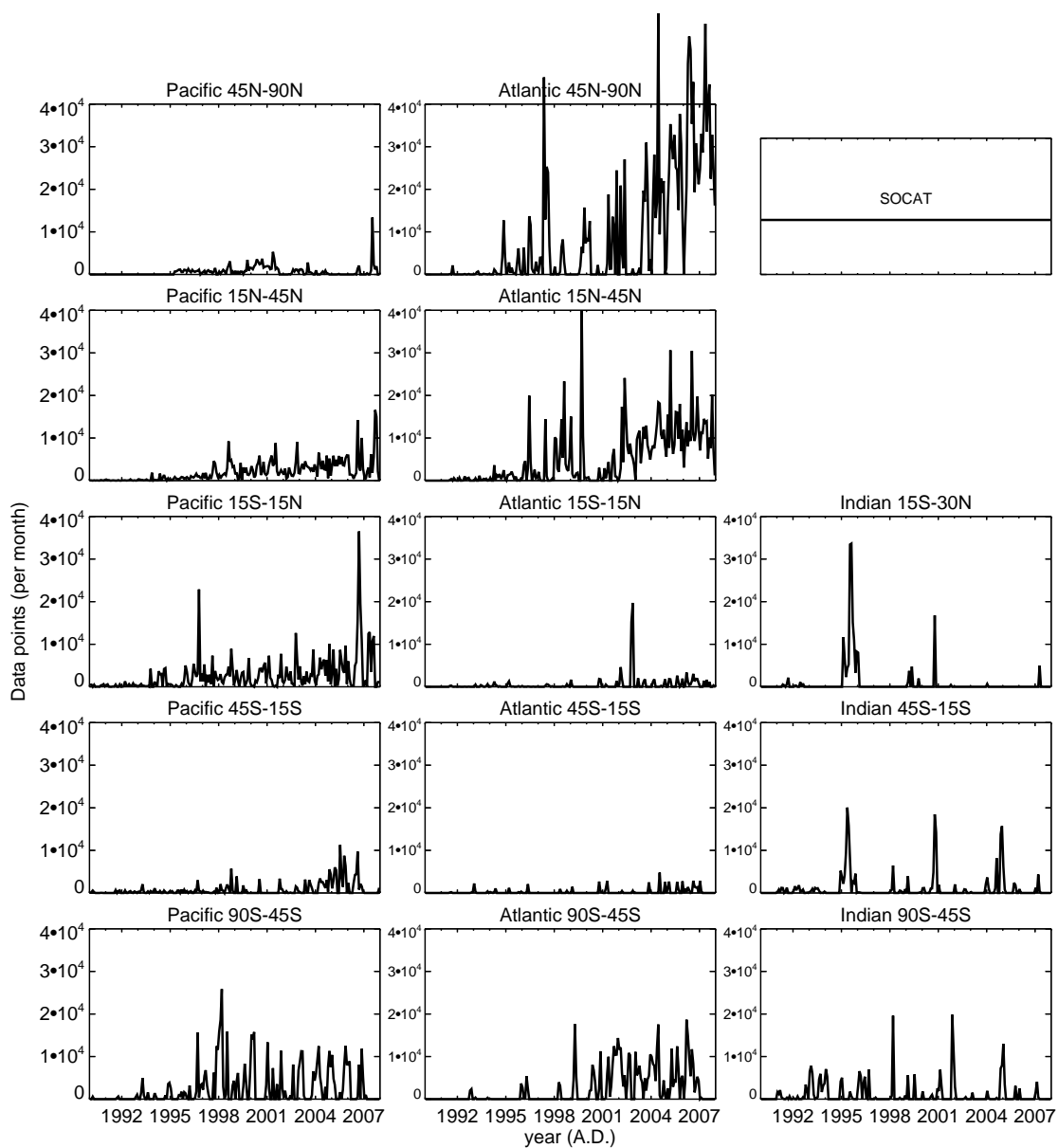


Fig. S7.3. Number of pixels with data points in the SOCAT data base for each month of the calculation. (Off-scale values in the North Atlantic are allowed for the sake of a more readable y scale.)

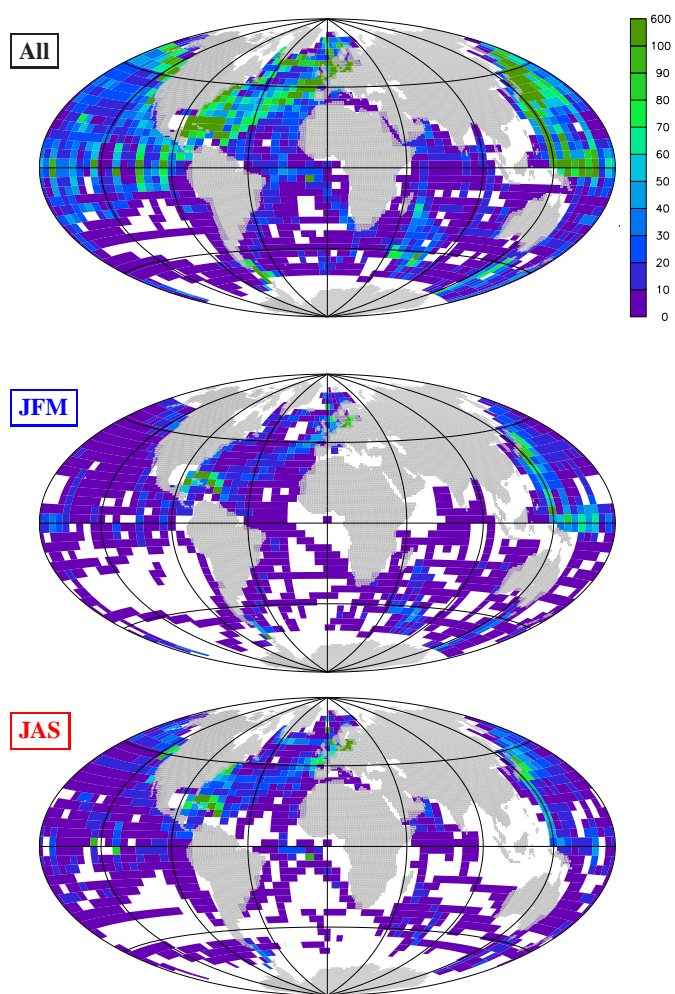


Fig. S7.4. Number of time steps where SOCAT data exist, during all the calculation period (top) or during (northern) winter (JFM, middle) or summer (JAS, bottom). White pixels have no data at all in the respective period.